



Nanoscale

Interaction of gases with monolayer WS₂: An In Situ Spectroscopy Study

Journal:	<i>Nanoscale</i>
Manuscript ID	NR-ART-03-2021-001483.R1
Article Type:	Paper
Date Submitted by the Author:	21-May-2021
Complete List of Authors:	Rao, Rahul; Air Force Research Laboratory Materials and Manufacturing Directorate Kim, Hyunil; Air Force Research Laboratory Materials and Manufacturing Directorate Lopez, Nestor Perea ; Penn State University, Physics Terrones, Mauricio; The Pennsylvania State University, Department of Physics; The Pennsylvania State University Maruyama, Benji; Air Force Research Laboratory, Materials and Manufacturing Directorate

SCHOLARONE™
Manuscripts

Interaction of gases with monolayer WS₂: An In Situ Spectroscopy Study

Rahul Rao^{1,*}, Hyunil Kim¹, Nestor Perea-López², Mauricio Terrones^{2,3,4}, Benji Maruyama¹

¹Materials and Manufacturing Directorate, Air Force Research Laboratory, Wright-Patterson AFB, OH 45433

²Department of Physics and Center for Two-Dimensional and Layered Materials, The Pennsylvania University, State College, PA

³Department of Materials Science and Engineering, The Pennsylvania State University, University Park, PA 16802, USA

⁴Department of Chemistry, The Pennsylvania State University, University Park, PA 16802, USA.

Abstract

The optical and electronic properties of two-dimensional (2D) materials can be tuned through physical and chemical adsorption of gases. They are also ideal sensor platforms, where charge transfer from the adsorbate can induce a measurable change in the electrical resistance within a device configuration. While 2D materials-based gas sensors exhibit high sensitivity, questions exist regarding the direction of charge transfer and the role of lattice defects during sensing. Here we measured the dynamics of adsorption of NO₂ and NH₃ on monolayer WS₂ using *in situ* photoluminescence (PL) and resonance Raman spectroscopy. Experiments were conducted across a temperature range of 25 – 250 °C and gas concentrations between 5 – 650 ppm. The PL emission energies blue- and red-shifted when exposed to NO₂ and NH₃, respectively, and the magnitude of the shift depended on the gas concentration as well as the temperature down to the lowest concentration of 5 ppm. Analysis of the adsorption kinetics revealed an exponential

* Correspondence: rahul.rao.2@us.af.mil

increase in the intensities of the trion peaks with temperature, with apparent activation energies similar to barriers for migration of sulfur vacancies in the WS_2 lattice. The corresponding Resonance Raman spectra allowed the simultaneous measurement of the defect-induced LA mode. A positive correlation between the defect densities and the shifts in the PL emission energies establish lattice defects such as sulfur vacancies as the preferential sites for gas adsorption. Moreover, an increase in defect densities with temperature in the presence of NO_2 and NH_3 suggests that these gases may also play a role in the creation of lattice defects. Our study provides key mechanistic insights into gas adsorption on monolayer WS_2 , and highlights the potential for future development of spectroscopy-based gas sensors based on 2D materials.

Introduction

Atomically thin two-dimensional (2D) materials possess high surface-to-volume ratios, making it possible to tune their properties through physical and chemical adsorption of gaseous molecules.^{1,2} The adsorption can induce charge transfer between the adsorbate and the 2D material, resulting in p- or n-type doping depending on the direction of charge (electron or hole) transfer. In a semiconducting device configuration, a small amount of adsorbed gas can result in a measurable change in electrical resistance, making monolayer 2D materials such as transition metal dichalcogenides (TMDs) ideal platforms for gas sensing.³⁻⁵ Indeed, sensing gases such as NO_2 at very high sensitivity (down to ppb-level concentrations) has been recently demonstrated in MoS_2 , boron-doped graphene and phosphorene.⁶⁻⁸ 2D materials are therefore ideally suited for detecting minute quantities of gases for environmental monitoring, process control, medical diagnostics and security.³⁻⁵

The overwhelming majority of studies on the interactions of gases with 2D materials have focused on electrical or electrochemical measurements.⁹ Depending on whether it is an electron donor or acceptor, the adsorbed gas causes an increase or decrease in electrical resistance, the magnitude of which depends on its concentration.¹⁰ The physical or chemical adsorption of the gas molecules typically occur on the basal plane of the semiconducting TMD; the process is reversible and induces charge transfer, resulting in a change in the electronic bandgap.¹¹ The

adsorption can also be measured by photoluminescence (PL) spectroscopy. The added electrons or holes in the monolayer also affect the neutral exciton (electron-hole pair) and charged exciton (neutral exciton with an extra electron or hole, also called trion) densities, which can be observed in the photoluminescence (PL) emission spectrum through shifts in the emission energies and exciton intensities. Recent experiments on monolayer MoS₂ have demonstrated a modulation of the exciton and trion intensities in the PL emission spectrum upon adsorption of 100 ppm of NO₂ and NH₃.¹²

Despite the numerous studies that have reported gas sensing in monolayer TMDs, discrepancies exist as to the mechanism and direction of charge transfer. For example, both increase and decrease in electrical resistance has been observed upon adsorption of H₂O onto monolayer WS₂, implying that H₂O can behave as an acceptor or a donor.¹³ These contrasting situations could be attributed to differences in the adsorption configurations of the H₂O molecules on the monolayer WS₂.¹⁴ On the other hand, these discrepancies could also occur due to defects (such as sulfur vacancies) in the monolayer and the manner of gas adsorption, physical or chemical.^{15,16} For example, previous studies have shown physisorption of NO₂ to be favorable on the basal plane of MoS₂, whereas it is chemisorbed on the edges.¹⁷ Theoretical and experimental studies have also shown that gas adsorption is higher at lattice defects such as sulfur vacancies.^{15,18}

To address these open questions, we used *in situ* photoluminescence and Raman spectroscopy to understand the interactions between NO₂ and NH₃ and monolayer WS₂ over a range of temperatures between 25 – 250 °C, and gas concentrations between 5 – 650 ppm. Our chosen temperature range was the typical operating range for gas sensors and similar devices. And while the limits of detection in our gas exposure experiments (5 and 15 ppm for NH₃ and NO₂, respectively) were on par with a large number of published gas sensing studies,^{3–5,9} our experiments were not conducted with the intention to maximize sensitivity, but to gain mechanistic insights into the interactions between the adsorbed gases and monolayer WS₂ through their optical and vibrational spectra.

In situ measurements of the exciton and trion emission energies and peak intensities revealed temperature- and concentration-dependent (down to the lowest concentration of 5

ppm) charge transfer between the gases and WS_2 through blue- and red-shifted PL emission energies for adsorption of NO_2 and NH_3 , respectively. Furthermore, we calculated apparent activation energies for the gas adsorption process from the *in situ* kinetics as well as near-resonance Raman spectra to measure defect densities and correlate the adsorption-induced PL emission energies to lattice defects in the monolayer WS_2 . Interestingly, we found that the gases also aid in the creation of defects, and this was proportional to the temperature. Our study highlights the power of Raman and PL spectroscopy to not only provide mechanistic insights into gas adsorption on 2D materials, but also the potential for the future development of spectroscopy-based gas sensors.

Experimental

Our gas adsorption and *in situ* spectroscopy measurements were conducted in a custom-built setup (called Autonomous Research System or ARES), which has previously been used to measure crystallization and defect generation kinetics in 2D materials like graphene, MoS_2 and $InSe$.^{19–25} In ARES, a 532nm laser (6W, Verdi) serves as both heat source and Raman/PL excitation source, and is focused on a silicon substrate consisting of patterned micropillars on an SiO_2 underlayer (10 μm in diameter and height, fabricated by reactive ion etching). The substrates are loaded into a miniature high vacuum chamber with an optical window and whose environment can be controlled through automated vacuum pumps and gas mass flow controllers. Heating of the thermally isolated micropillars is achieved by varying the laser power, allowing rapid increases (within microseconds) in temperatures up to 1200 °C with approximately 200 mW laser power at the sample. The scattered light from the micropillars is coupled to a spectrometer through focusing optics and a notch filter, enabling *in situ* Raman and photoluminescence measurements. The micropillar temperature is estimated from the redshifted Raman peak frequency of Si.^{24,26} For this study, monolayer WS_2 crystals were synthesized by chemical vapor deposition and transferred onto the ARES micropillars using the techniques described in Refs. 27 and 28. Scanning electron microscope images of fully and partially coated micropillars with transferred monolayer WS_2 are shown in Fig. S1 in the Electronic Supplementary Information.

The image of the partially coated micropillar is included just to show the difference in contrast between the WS₂ and the underlying silicon. All the *in situ* measurements were performed on fully coated micropillars. For the gas adsorption experiments, samples were loaded into the reactor and pumped down to the base pressure (10⁻⁶ Torr), followed by backfilling with the appropriate amounts of NO₂ or NH₃ (5 – 650 ppm). Fully coated micropillars were then heated up to the desired temperature (between 25 – 250 °C) and held for 90 – 120 s. Raman and PL spectra were collected continuously (typical spectral acquisition times were 3-5 s), and the spectra were fit to Lorentzian peaks to calculate intensities, frequencies and widths. Additional experiments were conducted where the temperature was cycled by increasing it to set values and cooling back down to room temperature.

Results and Discussion

Figure 1 shows PL emission spectra from monolayer WS₂ exposed to 65 ppm NO₂ and NH₃, and annealed for ~ 90 s at 80 and 120 °C, respectively. The spectra were collected every 4 s, and are plotted in Figs. 1a and 1b with increasing time from bottom to top. Before and after each experiment, a Raman spectrum was collected at a low excitation power (0.2 W, 30 s acquisition time) corresponding to room temperature; these spectra (pre- and post-scans) are plotted on the bottom and top of Figs. 1a and 1b. As expected, the waterfall plots in Fig. 1 show redshifts in the emission upon heating, which is consistent with temperature-induced bandgap reduction.^{29,30} The emission spectra also retained their position and lineshapes during the 90 s gas exposure, which suggests that the absorption did not change significantly during the 90 s timeframe.

The biggest difference due to gas exposure was revealed in the lineshape of the post-scan compared to the pre-scan. To see this difference, the pre- and post-scans were fit with two Lorentzian peaks following a baseline subtraction, and the results of the fits are shown in Figs. 1c and 1d for NO₂ and NH₃, respectively. The two fitted peaks correspond to emission due to recombination of neutral excitons (X) and charged excitons or trions (T). Firstly, the pre-scans shown in Figs. 1c and 1d exhibit subtle differences in the intensities of the trion and exciton peaks. This suggests a variation in the charge densities across the as-deposited monolayer WS₂ (in our

case variations across the ARES micropillars), which could arise from the synthesis or transfer process (Fig. S1). Secondly, and more importantly, the post-scans exhibit clear differences in the relative intensities of the trion and exciton peaks. For NO_2 , the exciton intensity increased after exposure, and the overall spectral weight blueshifted in energy (Fig. 1c). It was the opposite for NH_3 – the trion intensity increased relative to the exciton peak, and was accompanied by an overall redshift in the emission energy after exposure. These changes can be attributed to charge transfer induced by the adsorption of the gas. NO_2 (NH_3) is an acceptor (donor), whose adsorption onto WS_2 results in p-type (n-type) doping, and the charge transfer is reflected in the changes in emission shown in Figs. 1c and 1d. Similar changes in the PL emission in monolayer MoS_2 due to NO_2 and NH_3 adsorption were previously reported by Cho *et al.*¹² We note that varying degrees of charge transfer from the SiO_2 substrate to the monolayer WS_2 could also exist³¹ but we accounted for these differences by measuring the PL emission spectra before and after each heating experiment, thereby ensuring that analysis took into consideration relative changes in the charge state with respect to the initial state.

The blue- and red-shifts due to adsorption of NO_2 and NH_3 , respectively, were found to be consistent across all the measured gas concentrations and annealing temperatures. At low temperatures, the shifts in the emission energies were also accompanied by an increase (decrease) in PL emission intensity due to p-type (n-type) doping, as reported previously³². But the magnitude of the shift and relative intensities of the exciton and trion intensities depended on both the gas concentration and on the annealing temperature. Fig. 2a shows the trion/exciton intensity ratios (calculated by fitting baselines and two Lorentzian peaks to each emission spectrum) before and after adsorption of 650 ppm NO_2 (top panel) and NH_3 (bottom panel). The slight differences in the initial charge densities are reflected in the variations in the trion/exciton intensity ratios before gas adsorption (grey squares in Fig. 2a). After gas exposure, however, the trion/exciton intensity ratios increased (red and blue square data in Fig. 2a) and the increase was greater at higher temperatures (indicated by the dashed vertical arrows). The higher trion intensities can be attributed to greater charge transfer (hole or electron) between the adsorbed gases and WS_2 . The data in Fig. 2a allude to an increase in gas adsorption with temperature, which is contrary to what is expected for physical adsorption.³³

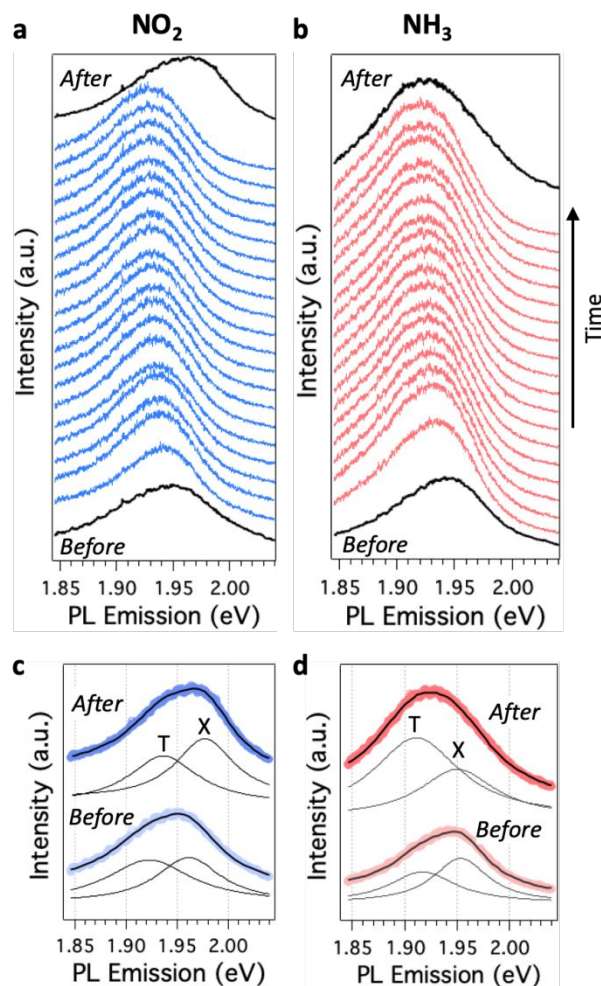


FIG. 1. *In situ* experiments in ARES. Waterfall plots showing PL emission spectra from monolayer WS_2 exposed to (a) NO_2 (65 ppm, 80 °C) and (b) NH_3 (65 ppm, 120 °C). PL emission spectra collected before and after gas exposure are shown in (c) and (d). The spectra are fitted to two Lorentzian peaks, corresponding to trion (T) and neutral exciton (X) emission.

From our *in situ* data, we were also able to measure the rates of increase in the trion intensities. An example of this is shown in the inset in Fig. 2b. In this experiment, the trion (exciton) intensity increased (decreased) over the duration of the exposure to NO_2 . The experimental data were fit with two exponential curves. We estimated the rates of increase of the trion peaks for all experiments, and the results are plotted in Fig. 2b for exposure to NO_2 (top) and NH_3 (bottom). All the data exhibited an exponential increase in the trion intensity with

temperature. The exciton peak intensities exhibited a concomitant exponential decrease. We fit the logarithms of the rates to an Arrhenius relationship against temperature with the form $A * e^{\left(-k_B/T\right)}$, where k_B and T are the Boltzmann constant and temperature, respectively, and A is a proportionality constant. These fits produced apparent activation energies ranging from 0.27 to 0.43 eV, with the lowest values for the highest gas concentrations. The energies were lower for NH_3 (0.27 – 0.3 eV) compared to NO_2 (0.36 – 0.43 eV), and could be attributed to differences in the activities of the two gases. Future theoretical investigations may shed more light on the mechanistic differences. But these energies are on par with previous reports of barriers for migration of sulfur vacancies ($\sim 0.5\text{-}0.6$ eV).^{34,35} The activation barriers are also expected to decrease in the case of pre-existing defects and this is discussed further below.

In addition to gas adsorption-induced changes in the trion and exciton intensities, our peak fitting analysis also revealed shifts in the energies of the exciton and trion emission peaks. These shifts were proportional to the gas concentration as well as the annealing temperature. For convenience, and to highlight the magnitude of shifts in the emission energies on gas concentration and temperature, we fit the emission peaks to a single Lorentzian peak, and plot the difference in the emission energies before and after gas exposure ($E_{\text{after}} - E_{\text{before}}$) in Fig. 2c. Some examples of shifts in both exciton and trion energies with temperature for a few gas concentrations are included in the ESI (Fig. S2). The graphs in Fig. 2c show blueshifted and redshifted emissions for exposure to NO_2 (top panel in Fig. 2c) and NH_3 (top panel in Fig. 2c), respectively. These shifts were also directly proportional to the gas concentration for a given temperature and increased with temperature, reaching a maximum blueshift (redshift) of ~ 30 meV (~ 40 meV) for exposure to NO_2 (NH_3) at the highest temperature.

The results presented in Fig 2. show clear evidence for concentration and temperature-dependent charge transfer due to adsorption of NO_2 and NH_3 . To see the reversibility of the adsorption process, we performed a series of thermal cycling experiments where the temperature was cycled by increasing to a set value, holding then decreasing to room temperature incrementally in high vacuum (10^{-5} Torr) as well as in the presence of Ar and NH_3 . Fig. 3a shows the variations in the trion and exciton energies with temperatures at 10^{-5} Torr.

During the course of this experiment, the temperature was alternated between room temperature and 150 °C (bottom panel, Fig. 3a). Both trion and exciton emission energies decreased concurrently with the increase in temperature from room temperature to 150 °C, but recovered to their original values upon cooling. The recovery of the PL emission energy indicates that there was no change in the charge state of the WS_2 on heating to at least 150 °C. In contrast to the behavior under vacuum, the PL emission energies did exhibit irreversible changes upon exposure to Ar (Fig. 3b) and NH_3 (Fig. 3c). In the case of 10 Torr Ar, we annealed incrementally up to 200 °C. The emission energies of the trion and exciton redshifted proportionally to the temperatures and did not go back to their room temperature values on cooling. In fact, the emission energies redshifted continuously even while the temperature was held constant at all values above room temperature. These irreversible effects were much worse for exposure to 650 ppm NH_3 , and accompanied by a higher redshift in the PL emission energies upon heating up to 150 °C.

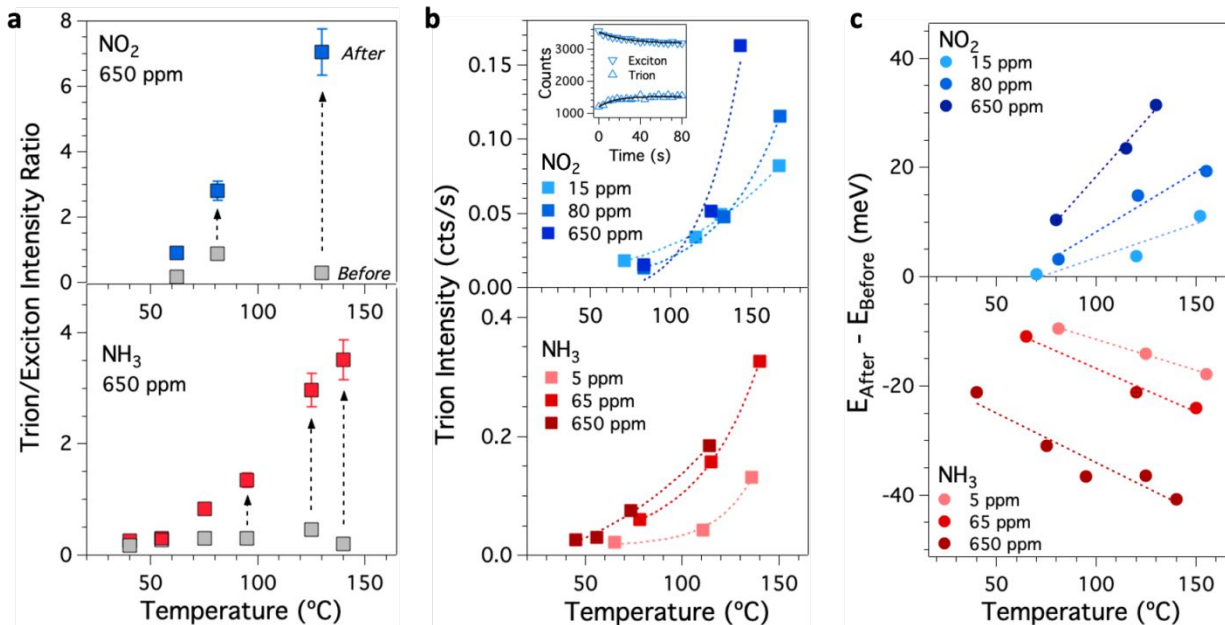


Fig. 2. (a) Trion/Exciton intensity ratios against temperature for exposure to 650 ppm NO_2 (top) and NH_3 (bottom). The ratios were calculated by fitting the emission spectra (collected at room temperature) to two Lorentzian peaks. Ratios before annealing are plotted in grey and after annealing in blue and red for NO_2 and NH_3 , respectively. (b) Rate of increase in trion intensity as

a function of temperature for exposure to NO_2 (top) and NH_3 (bottom). The exciton (trion) intensity decreased (increased) exponentially with temperature, an example of which is shown in the inset. (c) Difference in emission energies before and after gas exposure as a function of gas concentration and temperature. Here the emission energies blueshifted and redshifted for exposure to NO_2 (top panel) and NH_3 (bottom panel), respectively. These shifts were directly proportional to both gas concentration and temperature.

The trends shown in Figs. 2 and 3 collectively point to defects as the cause of the shifts and irreversibility observed in the PL emission. Lattice defects such as sulfur vacancies are known to be generated on annealing monolayer TMDs at elevated temperatures. Previous reports have shown that vacuum annealing of WS_2 and MoS_2 up to $250\text{ }^\circ\text{C}$ does not result in any structural defects, but heating to higher temperatures (up to $600\text{ }^\circ\text{C}$) significantly increases the number of sulfur vacancies.^{36,37} This would explain our observation of full PL recovery during vacuum annealing (Fig. 3a). However, the irreversible redshifts of the PL emission while heating under Ar and NH_3 are likely due to the generation of sulfur vacancies. We have previously shown a direct correlation between redshifted PL emission energies and defect densities due to sulfur vacancies in monolayer MoS_2 .³⁸ Our observation of greater redshifts in the PL emission energies upon exposure of WS_2 to NH_3 compared to Ar at the same temperature (Figs. 3b and 3c) indicate higher defect densities due to NH_3 . Note that in the case of 10 Torr Ar, there might be residual oxygen generating the sulfur vacancies.³⁸ In general, an increase in defects would lead to greater chemisorption of NH_3 and NO_2 , as previously reported.^{16,39} This in turn would cause the poor recovery of the PL emission energies upon cooling down to room temperature.

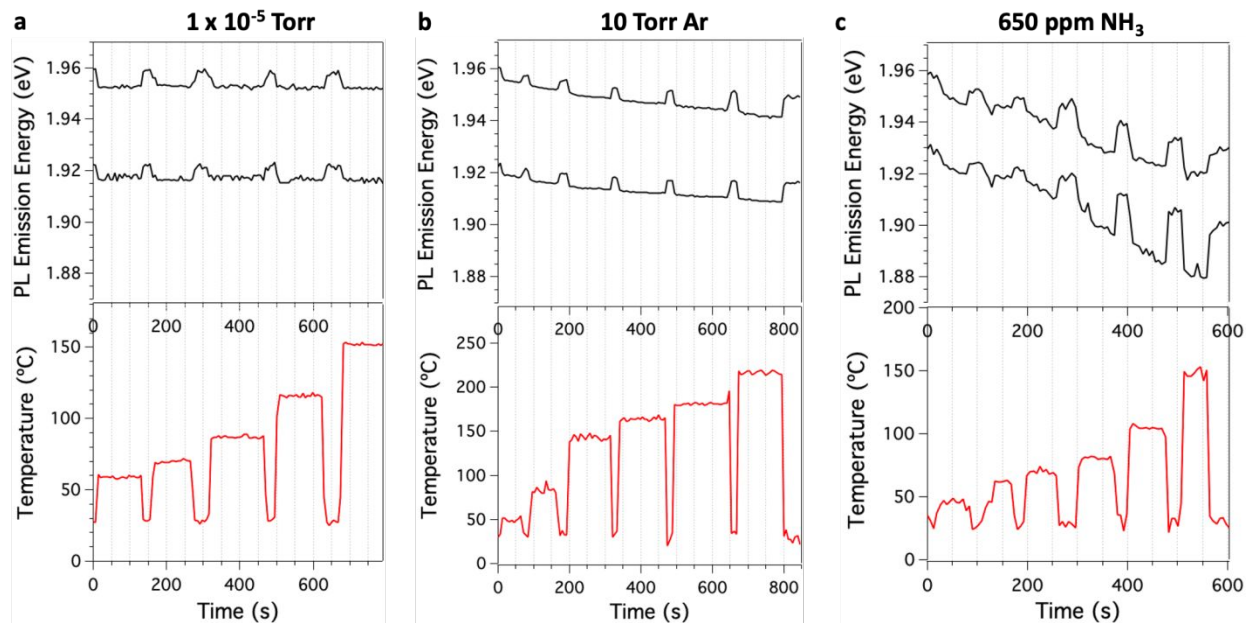


Fig. 3. Thermal cycling of the PL emission energies. Variation in exciton and trion emission energies (top panels) over time as the temperature (bottom panels) was increased and lowered incrementally for monolayer WS_2 in (a) 10^{-5} Torr vacuum, (b) 10 Torr Ar, and (c) 650 ppm NH_3 . Changes in the PL emission were most severe for exposure to NH_3 and less severe under an Ar environment. No change to the PL emission was observed under vacuum up to 150 °C.

To test our hypothesis, we turned to resonance Raman spectroscopy. Excitation with a laser energy close to the optical gap of monolayer WS_2 (~ 2 eV), for example with 532 nm (2.33 eV), reveals a rich Raman spectrum containing several non-zone center phonon modes and higher order combination modes.⁴⁰ Among these, a longitudinal acoustic (LA) mode appears as a result of defect-mediated scattering of the excitation photon with zone boundary phonons.^{41,42} This mode could arise from the M or K point of the WS_2 Brillouin zone,⁴³ and for brevity we call it the LA mode. The exact type of the defect responsible for the appearance of this peak is under investigation. However, its intensity has been correlated previously to sulfur vacancies and the ratio of intensities of the LA mode with respect to the zone-center E' or A' modes ($I_{LA}/I_{E'}$ or $I_{LA}/I_{A'}$) has been used to qualitatively monitor the sulfur vacancy concentration in monolayer MoS_2 and WS_2 .^{38,44–47}

Figure 4a shows representative Raman spectra collected before and after exposure (*i.e.* pre- and post-scan) to 650 ppm NH_3 (annealed at 95 °C). The peak around 180 cm^{-1} is the LA

mode, and the broader peak around 350 cm^{-1} is its overtone ($2LA$). The $2LA$ mode is very intense for monolayer WS_2 when using 532 nm excitation owing to the double resonance process.^{40,48} The frequency of the in-plane vibrational mode of WS_2 (E') overlaps with the $2LA$ mode in the near-resonance Raman spectrum. But peak fitting reveals the two distinct E' and $2LA$ peaks, as shown in Fig. 4a. Note that the presence of the LA mode in the pre-scan indicates that defects are already present in the as-deposited material, which is expected in CVD-grown (and transferred) monolayer TMDs.^{49–51} Similar to the case of MoS_2 ,^{38,44} we calculated the defect densities from the ratios of the areas of the LA and the E' modes, and subtracted the value before gas adsorption from the density after gas adsorption (spectra collected at room temperature). The resulting difference values (ΔLA) are plotted against temperature in Fig. 4b for exposure of monolayer WS_2 to 650 ppm of NO_2 and NH_3 . First, all the ΔLA values in Fig. 4b are positive, implying an increase in defect density after exposure to both NO_2 and NH_3 . Second, the defect densities increased with temperature by a factor of six, from ~ 0.15 up to ~ 0.9 , and the effect was greater for NH_3 compared to NO_2 . As mentioned above, lattice defects such as sulfur vacancies are typically generated on heating monolayer TMDs to much higher temperatures (closer to $600\text{ }^\circ\text{C}$). Our observation of increasing defects upon annealing to $150\text{ }^\circ\text{C}$ therefore ostensibly implicates NO_2 and NH_3 as being responsible for defect generation in the monolayer WS_2 . We therefore hypothesize that sulfur vacancies are generated in the presence of the gases; this effect increases with temperature and results in an increase in adsorbed gas owing to their higher binding affinity to chalcogen vacancies.¹⁵ Our hypothesis is supported by our observation of an increase in the LA peak intensity as well as the activation energies obtained by analyzing the rates of increases in the trion peak intensities. Further experimental and theoretical investigations will be needed for verification. We also note that lattice strain imparted due to the transfer and heating of the micropillar could impact the gas adsorption and can be observed through the significant broadening of Raman peaks and redshifts of PL emission energies.^{52–55} While we cannot preclude these effects, we did not observe significant broadening in the Raman spectra (Fig.4a and S3) or redshifted PL emission (evidenced in Fig. 3a by the steady recovery of the exciton and trion emission upon rapid heating and cooling under vacuum) before and after heating indicative of strain. Moreover, as mentioned above, such effects can be mitigated by

measuring spectra before and after gas exposure from the same regions. Finally, unlike our previous observation of photothermal dissociation of O_2 resulting in defects in graphene,⁵⁶ NO_2 and NH_3 are expected to dissociate with UV excitation,^{57,58} not visible light. Thus, our observations of defect generation and doping in WS_2 upon gas adsorption can be attributed mainly to the interactions between the gases and the WS_2 lattice.

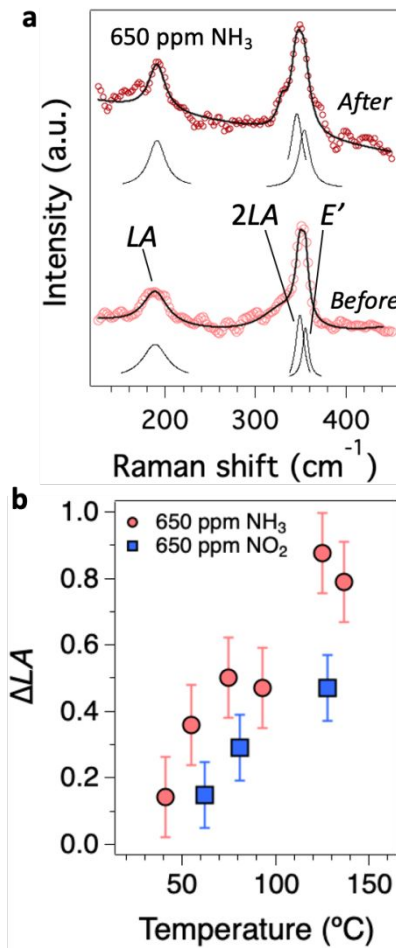


Fig. 4. Effect of defect density on gas adsorption. (a) Representative Raman spectra collected before (bottom) and after (top) exposure of monolayer WS_2 to 650 ppm NH_3 . The defect-induced LA(M) peaks and the $E' + 2LA(M)$ peaks are indicated. The LA(M) peak intensity increased after gas exposure. (b) Change in the defect density (ΔLA) after exposure to 650 ppm NO_2 and NH_3 . The increase in defect density with temperature corroborates the blue- and red-shifted PL emission energies due to adsorption of NO_2 and NH_3 , respectively (Fig. 2).

Conclusions

We studied the interaction between NO_2 and NH_3 with monolayer WS_2 using *in situ* PL and Raman spectroscopy. Gas adsorption experiments were conducted for a variety of gas concentrations (5 – 650 ppm) between 20 and 250 °C. The PL emission energies blue- and red-shifted for exposure to NO_2 and NH_3 , respectively, due to charge transfer from the gases upon adsorption. These shifts were proportional to the concentration and temperature. The charge transfer from the gases was also revealed in an exponential increase in trion peak intensity, with activation energies corresponding to migration of sulfur vacancies. The generation of sulfur vacancies (and other possible lattice defects) was also revealed by analysis of resonance Raman spectra, with a positive correlation between the defect density and the observed shifts in PL emission energies. Our studies revealed that, while monolayer WS_2 shows potential for gas sensing via adsorption, the interaction between NO_2 and NH_3 at elevated temperatures can also result in lattice defects such as sulfur vacancies. These results suggest lower operating temperatures for gas sensors based on 2D materials. Moreover, we show the potential for future development of spectroscopy-based gas sensors.

References

- 1 S. Bertolazzi, M. Gobbi, Y. Zhao, C. Backes and P. Samorì, *Chem. Soc. Rev.*, 2018, **47**, 6845–6888.
- 2 P. Luo, F. Zhuge, Q. Zhang, Y. Chen, L. Lv, Y. Huang, H. Li and T. Zhai, *Nanoscale Horiz.*, 2019, **4**, 26–51.
- 3 S. Yang, C. Jiang and S. Wei, *Appl. Phys. Rev.*, 2017, **4**, 021304.
- 4 X. Liu, T. Ma, N. Pinna and J. Zhang, *Adv. Funct. Mater.*, 2017, **27**, 1702168.
- 5 W. Yang, L. Gan, H. Li and T. Zhai, *Inorg. Chem. Front.*, 2016, **3**, 433–451.
- 6 T. Pham, G. Li, E. Bekyarova, M. E. Itkis and A. Mulchandani, *ACS Nano*, 2019, **13**, 3196–3205.
- 7 R. Lv, G. Chen, Q. Li, A. McCreary, A. Botello-Méndez, S. V. Morozov, L. Liang, X. Declerck, N. Perea-López, D. A. Cullen, S. Feng, A. L. Elías, R. Cruz-Silva, K. Fujisawa, M. Endo, F. Kang, J.-C. Charlier, V. Meunier, M. Pan, A. R. Harutyunyan, K. S. Novoselov and M. Terrones, *Proc. Natl. Acad. Sci.*, 2015, **112**, 14527.
- 8 S. Cui, H. Pu, S. A. Wells, Z. Wen, S. Mao, J. Chang, M. C. Hersam and J. Chen, *Nat. Commun.*, 2015, **6**, 8632.
- 9 M. Donarelli and L. Ottaviano, *Sensors*, 2018, **18**, 3638.
- 10 D. J. Late, Y.-K. Huang, B. Liu, J. Acharya, S. N. Shirodkar, J. Luo, A. Yan, D. Charles, U. V. Waghmare and V. P. Dravid, *ACS Nano*, 2013, **7**, 4879–4891.
- 11 C. Zhou, W. Yang and H. Zhu, *J. Chem. Phys.*, 2015, **142**, 214704.
- 12 B. Cho, M. G. Hahm, M. Choi, J. Yoon, A. R. Kim, Y.-J. Lee, S.-G. Park, J.-D. Kwon, C. S. Kim and M. Song, *Sci. Rep.*, 2015, **5**, 8052.
- 13 N. Huo, S. Yang, Z. Wei, S.-S. Li, J.-B. Xia and J. Li, *Sci. Rep.*, 2014, **4**, 5209.
- 14 V. Q. Bui, T.-T. Pham, D. A. Le, C. M. Thi and H. M. Le, *J. Phys. Condens. Matter*, 2015, **27**, 305005.
- 15 H. Li, M. Huang and G. Cao, *Phys. Chem. Chem. Phys.*, 2016, **18**, 15110.
- 16 D. Ma, B. Ma, Z. Lu, C. He, Y. Tang, Z. Lu and Z. Yang, *Phys. Chem. Chem. Phys.*, 2017, **19**, 26022–26033.
- 17 J. Huang, J. Chu, Z. Wang, J. Zhang, A. Yang, X. Li, C. Gao, H. Huang, X. Wang, Y. Cheng and M. Rong, *ChemNanoMat*, 2019, **5**, 1123–1130.
- 18 Y. Xia, C. Hu, S. Guo, L. Zhang, M. Wang, J. Peng, L. Xu and J. Wang, *ACS Appl. Nano Mater.*, 2020, **3**, 665–673.
- 19 K. Share, R. E. Carter, P. Nikolaev, D. Hooper, L. Oakes, A. P. Cohn, R. Rao, A. A. Puzos, D. B. Geohegan, B. Maruyama and C. L. Pint, *J. Phys. Chem. C*, 2016, **120**, 14180–14186.
- 20 R. Rao, A. E. Islam, P. M. Campbell, E. M. Vogel and B. Maruyama, *2D Mater.*, 2017, **4**, 025058.
- 21 R. A. Vilá, R. Rao, C. Muratore, E. Bianco, J. A. Robinson, B. Maruyama and N. R. Glavin, *2D Mater.*, 2017, **5**, 011009.
- 22 H. Bergeron, L. M. Guiney, M. E. Beck, C. Zhang, V. K. Sangwan, C. G. Torres-Castaneda, J. T. Gish, R. Rao, D. R. Austin, S. Guo, D. Lam, K. Su, P. T. Brown, N. R. Glavin, B. Maruyama, M. J. Bedzyk, V. P. Dravid and M. C. Hersam, *Appl. Phys. Rev.*, 2020, **7**, 041402.
- 23 R. Rao, D. Liptak, T. Cherukuri, B. I. Yakobson and B. Maruyama, *Nat. Mater.*, 2012, **11**, 1–4.
- 24 P. N. Nikolaev, D. Hooper, F. Webber, R. Rao, K. Decker, M. Krein, J. Poleski, R. Barto and B. Maruyama, *Npj Comput. Mater.*, 2016, **2**, 16031.

- 25E. J. Kluender, J. L. Hedrick, K. A. Brown, R. Rao, B. Meckes, J. S. Du, L. M. Moreau, B. Maruyama and C. A. Mirkin, *Proc. Natl. Acad. Sci.*, 2019, **116**, 40–45.
- 26R. Tsu and J. G. Hernandez, *Appl. Phys. Lett.*, 1982, **41**, 1016.
- 27J. T. Mlack, P. Masih Das, G. Danda, Y.-C. Chou, C. H. Naylor, Z. Lin, N. P. López, T. Zhang, M. Terrones, A. T. C. Johnson and M. Drndić, *Sci. Rep.*, 2017, **7**, 43037.
- 28A. L. Elías, N. Perea-López, A. Castro-Beltrán, A. Berkdemir, R. Lv, S. Feng, A. D. Long, T. Hayashi, Y. A. Kim, M. Endo, H. R. Gutiérrez, N. R. Pradhan, L. Balicas, T. E. Mallouk, F. López-Urías, H. Terrones and M. Terrones, *ACS Nano*, 2013, **7**, 5235–5242.
- 29Y. P. Varshni, *Physica*, 1967, **34**, 149–154.
- 30K. P. O'Donnell and X. Chen, *Appl. Phys. Lett.*, 1991, **58**, 2924–2926.
- 31J. Miao, X. Liu, K. Jo, K. He, R. Saxena, B. Song, H. Zhang, J. He, M.-G. Han, W. Hu and D. Jariwala, *Nano Lett.*, 2020, **20**, 2907–2015.
- 32S. Mouri, Y. Miyauchi and K. Matsuda, *Nano Lett.*, 2013, **13**, 5944–5948.
- 33N. Aguilar and S. Aparicio, *J. Phys. Chem. C*, 2019, **123**, 26338–26350.
- 34H.-P. Komsa, S. Kurasch, O. Lehtinen, U. Kaiser and A. V. Krasheninnikov, *Phys. Rev. B*, 2013, **88**, 035301.
- 35M. Precner, T. Polaković, Q. Qiao, D. Trainer, A. Putilov, C. Di Giorgio, I. Cone, Y. Zhu, X. Xi and M. Iavarone, *Sci. Rep.*, 2018, **8**, 1–10.
- 36B. Schuler, D. Y. Qiu, S. Refaely-Abramson, C. Kastl, C. T. Chen, S. Barja, R. J. Koch, D. F. Ogletree, S. Aloni, A. M. Schwartzberg, J. B. Neaton, S. G. Louie and A. Weber-Bargioni, *Phys. Rev. Lett.*, 2019, **123**, 076801.
- 37M. Liu, J. Shi, Y. Li, X. Zhou, D. Ma, Y. Qi, Y. Zhang and Z. Liu, *Small*, 2017, **13**, 1602967.
- 38R. Rao, V. Carozo, Y. Wang, A. E. Islam, N. Perea-Lopez, K. Fujisawa, V. H. Crespi, M. Terrones and B. Maruyama, *2D Mater.*, 2019, **6**, 045031.
- 39D. Burman, R. Ghosh, S. Santra, S. K. Ray and P. K. Guha, *Nanotechnology*, 2017, **28**, 435502.
- 40A. Berkdemir, H. R. Gutierrez, A. R. Botello-Méndez, N. Perea-Lopez, A. L. Elías, C.-I. Chia, B. Wang, V. H. Crespi, F. López-Urías, J.-C. Charlier, H. Terrones and M. Terrones, *Sci. Rep.*, 2013, **3**, 1755.
- 41G. Frey, R. Tenne, M. Matthews, M. Dresselhaus and G. Dresselhaus, *J. Mater. Res.*, 1998, **13**, 2412–2417.
- 42A. Stacy and D. Hodul, *J. Phys. Chem. Solids*, 1985, **46**, 405–409.
- 43C. Sourisseau, F. Cruege, M. Fouassier and M. Alba, *Chem. Phys.*, 1991, **150**, 281–293.
- 44S. Mignuzzi, A. J. Pollard, N. Bonini, B. Brennan, I. S. Gilmore, M. A. Pimenta, D. Richards and D. Roy, *Phys. Rev. B*, 2015, **91**, 195411.
- 45M. Zhang, M. Lihter, M. Macha, K. Banjac, Y. Zhao, Z. Wang, J. Zhang, J. Comtet, M. Lingenfelder and A. Kis, *ArXiv Prepr. ArXiv200612181*.
- 46A. McCreary, A. Berkdemir, J. Wang, M. A. Nguyen, A. L. Elías, N. Perea-López, K. Fujisawa, B. Kabius, V. Carozo, D. A. Cullen, T. E. Mallouk, J. Zhu and M. Terrones, *J. Mater. Res.*, 2016, **31**, 931–944.
- 47Z. Lin, B. R. Carvalho, E. Kahn, R. Lv, R. Rao, H. Terrones, M. E. Pimenta and M. Terrones, *2D Mater.*, 2016, **3**, 022002.
- 48R. N. Gontijo, G. C. Resende, C. Fantini and B. R. Carvalho, *J. Mater. Res.*, 2019, **34**, 1976–1992.

- 49W. Zhou, X. Zou, S. Najmaei, Z. Liu, Y. Shi, J. Kong, J. Lou, P. M. Ajayan, B. I. Yakobson and J.-C. Idrobo, *Nano Lett.*, 2013, **13**, 2615–2622.
- 50J. Hong, Z. Hu, M. Probert, K. Li, D. Lv, X. Yang, L. Gu, N. Mao, Q. Feng, L. Xie, J. Zhang, D. Wu, Z. Zhang, C. Jin, W. Ji, X. Zhang, J. Yuan and Z. Zhang, *Nat. Commun.*, 2015, **6**, 6293.
- 51V. Carozo, Y. Wang, K. Fujisawa, B. R. Carvalho, A. McCreary, S. Feng, Z. Lin, C. Zhou, N. Perea-López, A. L. Elías, B. Kabius, V. H. Crespi and M. Terrones, *Sci. Adv.*, 2017, **3**, e1602813.
- 52R. Rao, A. E. Islam, S. Singh, R. Berry, R. K. Kawakami, B. Maruyama and J. Katoch, *Phys Rev B*, 2019, **99**, 195401.
- 53T. Darlington, A. Krayev, V. Venkatesh, R. Saxena, J. W. Kysar, N. J. Borys, D. Jariwala and J. Schuck, *J. Chem. Phys.*, 2020, **153**, 024702.
- 54Y. Wang, C. Cong, W. Yang, J. Shang, N. Peimyoo, Y. Chen, J. Kang, J. Wang, W. Huang and T. Yu, *Nano Res.*, 2015, **8**, 2562–2572.
- 55S. Hao, B. Yang and Y. Gao, *RSC Adv.*, 2016, **6**, 59816–59822.
- 56A. E. Islam, S. S. Kim, R. Rao, Y. Ngo, J. Jiang, P. Nikolaev, R. R. Naik, R. Pachter, J. Boeckl and B. Maruyama, *RSC Adv.*, 2016, **6**, 42545–42553.
- 57I. Wilkinson, I. A. Garcia, B. J. Whitaker, J.-B. Hamard and V. Blanchet, *Phys. Chem. Chem. Phys.*, 2010, **12**, 15766–15779.
- 58H. Okabe and M. Lenzi, *J. Chem. Phys.*, 1967, **47**, 5241–5246.